Aalborg Universitet

AALBORG UNIVERSITY
DENMARK

Sub-synchronous Oscillation Characteristics and Analysis of Direct-drive Wind Farms with VSC-HVDC Systems

Shao, Bingbing; Zhao, Shuqiang; Yang, Y.; Gao, Benfeng; Blaabjerg, F.

Link to publication from Aalborg University

Sub-synchronous Oscillation Characteristics and Analysis of Direct-Drive Wind Farms with VSC-HVDC Systems

Bingbing Shao, *Student Member, IEEE*, Shuqiang Zhao, Yongheng Yang, *Senior Member, IEEE*, Benfeng Gao, and Frede Blaabjerg, *Fellow, IEEE*

Abstract—**Field experiences have shown that sub-synchronous oscillations (SSOs) can occur in direct-drive wind farms with VSC-HVDC (DDWFV) systems. In light of this, a dynamic mathematical model of the DDWFV is established in this paper. The SSO characteristics are analyzed through the eigenvalue method. Considering the participation factor, the analysis reveals that the SSO is mainly affected by the grid-side converter controller of the wind turbine units, the rectifier controller of the VSC-HVDC and certain system parameters. The impact of system parameters on the damping performance and frequency characteristics of the SSO is further explored. By separating the VSC-HVDC into three parts, the impact of the control characteristics and the AC-side elements characteristics of the VSC-HVDC on the SSO is discussed. New insights into the SSO issue are also offered by analyzing the interaction among various state variables. The theoretical analysis is verified by extensive time-domain simulations.**

Index Terms—**eigenvalue, mechanism, source-network-control, sub-synchronous oscillation, VSC-HVDC.**

I. INTRODUCTION

DUE to restriction on land space and wind energy sources, large-scale offshore wind farms are deployed far from the main power nodes. Large-capacity and long-distance offshore wind power transmission is dominating the wind energy system [1]. When the transmission distance is longer than 90 km (common in offshore wind farms), the high-voltage direct current (HVDC) transmission is more economical and reliable than AC transmission [2]. Additionally, the voltage source converter (VSC)-based HVDC technology has the advantages like being able to provide long-distance transmission without additional filtering devices. Hence, the VSC-HVDC has been increasingly used in offshore wind farms for power transmission [3]. As for the offshore generators, the direct-drive permanent magnet synchronous generator (D-PMSG) without gearboxes and any excitation control system is reliable and effective. That is, the D-PMSG becomes much preferable in offshore wind power systems [4].

B. Shao, S. Zhao, and B. Gao are with the Key Laboratory of Distributed Energy Storage and Microgrid of Hebei Province (North China Electric Power University), Baoding 071003, Hebei Province, China (e-mail: shaobingbing1223@163.com; zsqdl@163.com; gaobenfeng@126.com).

Y. Yang and F. Blaabjerg are with the Department of Energy Technology, Aalborg University, Aalborg 9220, Denmark (e-mail: yoy@et.aau.dk; fbl@et.aau.dk).

Direct-drive wind farms with the VSC-HVDC (DDWFV) is therefore one of the promising wind energy solutions.

At present, the Zhangbei DC power grid project in China and the Borwin1 project in Germany [5] are representatives of the wind farms with VSC-HVDC systems. However, as reported in [6], sub-synchronous oscillations (SSOs) occurred in wind farms with VSC-HVDC systems in China. In addition, the medium-frequency oscillation of 250-350 Hz has occurred in Borwin1 [5], and high-frequency oscillation of 1270 Hz has been seen between the ±350-kV/1000-MW Luxi VSC-HVDC converter and the 525-kV AC grid after the disconnection of several AC transmission lines [7]. Thus, it is of significance to study the stability of the DDWFV, which will be the focus of this paper.

Significant efforts have been devoted to the stability of grid-connected D-PMSG and VSC-HVDC systems in the literature. When D-PMSG wind farms are connected to series-compensated system or a weak AC grid, the small-signal stability was investigated in [8], [9] and [10]-[12], respectively. In addition, the stability of the VSC-HVDC system without wind farms has been studied by analyzing the eigenvalues, impedance or based on nonlinear analysis methods [13]-[16]. In [8]-[16], the impact of system parameters or control parameters on the stability was investigated considering D-PMSG wind farms or the VSC-HVDC, separately. Yet, the above analysis has not considered D-PMSG wind farms with VSC-HVDC systems. The instability mechanisms in [8]-[16] are different from that in wind farms with VSC-HVDC systems. For wind farms connected to series-compensated systems, the instability results from the interaction between the controllers of wind farms and the series-compensated system [9]. For wind farms connected to a weak AC grid, the instability is due to the interaction between the controllers of wind farms and the weak AC grid [10]. For the VSC-HVDC system alone, the interaction between the controllers of the VSC-HVDC and the weak AC grid [16] or harmonic resonance from the DC system may cause the instability [14]. However, the SSO in wind farms with VSC-HVDC systems mainly results from the interaction between the controllers of wind farms and the rectifier (REC) controller of the VSC-HVDC. Thus, the feasibility of the above analysis should be reevaluated in wind farms with VSC-HVDC systems. The characteristics of the SSO, medium-frequency oscillation and harmonic resonances in doubly fed induction generator (DFIG) wind farms with the VSC-HVDC were analyzed in [17]-[19]. As the operating characteristics and structure of the D-PMSG are different from those of the DFIG, the stability of the DDWFV should be further explored.

This paper focuses on the SSO characteristics and mechanism seen from the small-signal-stability point of view, and thus, the bifurcation and chaos of the DDWFV [20] are not concerned. Two main methods have been widely used to analyze the power system small-signal stability [21], i.e., the impedance analysis [22] and the eigenvalue method [13]. The open-loop modal method [23] and the amplitude-phase dynamics method [24] were also developed to analyze the small-signal stability. So far, only the impedance analysis, eigenvalue method and open-loop modal method have been used to explore the small-signal stability of the DDWFV [25]-[41].

For the impedance analysis, the impedance models of two subsystems are firstly established [42]. Then, the small-signal stability is analyzed according to the Nyquist or generalized Nyquist criterion. To analyze the oscillation characteristics, the impedance analysis in [25]-[34] was applied to obtain the impedance of the DDWFV. Then, the impact of the output active power, AC filters, controller parameters of D-PMSGs and VSC-HVDC was investigated. Furthermore, as indicated in [30], the bandwidth ratio between the grid-side converter (GSC) of D-PMSGs and REC of the VSC-HVDC plays a vital role in the root cause of the SSO. In [35], [36], the interactions between the HVDC converter control and electrical resonances of offshore grids were analyzed, but the resonances in the sub-synchronous frequency region were not concerned. In [37], the dynamic characteristics of the VSC-HVDC system were studied, but the wind farm was represented by an ideal current source. This implies that the dynamic characteristics of the wind farm were ignored and only the impacts on the power flow were reserved. Considering this issue, the DC impedance of the wind farm-connected VSC-HVDC was developed in [41] by harmonic transfer functions, and then the impact of the number of wind turbines and controller parameters on the DC system stability was investigated. However, the DC-side harmonic resonance [41] is different from the SSO mechanism discussed in this paper. Based on the impedance analysis method, the interaction between the wind farm subsystem and the VSC-HVDC is reflected by the established impedance models. However, the two subsystems are presented in the simplified form of an *R-C* (a resistance in series with a capacitance) or *R-L* (a resistance in series with an inductance) circuit [18]. This implies that the oscillation characteristics within the two subsystems cannot be reflected in detail.

The eigenvalue analysis method is an effective method that is suitable for multi-input-multi-output (MIMO) systems. It provides the root locus in various operating conditions, and it is more intuitive and has a useful feature "participation factor analysis" compared to the impedance analysis. For instance, the eigenvalue method was applied in [38], [39], where the impact of the output active power, GSC and phase-locked loop (PLL) parameters of PMSGs as well as filter parameters on the stability of the DDWFV was investigated. This method can be used to obtain the oscillation modes and determine the physical components of interest. However, how the interactions of the components result in instability cannot be revealed [43], as the eigenvalue method is a numerical solution without detailed physical meanings [18], [24]. Hence, it has difficulties for the SSO mechanism analysis [13].

The open-loop modal method is based on the modal analysis of two open-loop subsystems. When the eigenvalues of the two subsystems are close, the sub-synchronous interaction (SSI) between the two subsystems may become strong to degrade the damping of the power system SSOs. With the open-loop modal method in [40], it was found that when the PMSGs participated in the open-loop modal couplings, strong SSIs between the converter control of the VSC-HVDC and the PMSGs caused the SSOs. Meanwhile, the impact of DC voltage control parameters on the open-loop modal coupling was investigated. However, like the impedance analysis method, the open-loop modal method should firstly divide the entire system into two subsystems, and then the interactions between the two are investigated from the standpoint of the system modal condition. This implies that the dynamic characteristics of each subsystem are presented in the form of eigenvalues, which results in the unclear dynamic interactions among the relevant state variables within the subsystem [13].

In brief, the major focus of the SSO analysis in the DDWFV has been put on the control parameters, while few system parameters are analyzed. In the planning phase of the DDWFV, the system parameters are generally designed according to certain principles without considering the impact on the stability [34]. Thus, the impact of the system parameters on the SSO characteristics should be analyzed to ensure the system stability during the planning phase. Then, repetitive redesigns which may incur higher costs can be avoided. In addition, when the VSC-HVDC is applied in grid-connected D-PMSGs system, how the system damping changes remains a question, and then whether to use the VSC-HVDC or AC lines in grid-connected D-PMSGs is unclear. To comprehensively understand the damping characteristics of the VSC-HVDC, the impact of the VSC-HVDC connection on the SSO characteristics should be analyzed. Also, the impedance analysis method, eigenvalue analysis method and open-loop modal method cannot reveal the interactions among relevant state variables in the DDWFV. The contributions of this paper are summarized as follows:

- The SSO characteristics are analyzed considering the system parameters, which guides the design of the DDWFV in the planning phase.
- The impact of the VSC-HVDC connection on the SSO characteristics is analyzed through eigenvalue method and time-domain simulations. The VSC-HVDC is divided into three parts: source, network, and control. Then, the impact of the AC-side elements and the control characteristics on the SSO characteristics is investigated.
- New insights into the SSO mechanism of the DDWFV are provided from the dynamic interactions among relevant state variables. Then, the entire dynamic process associated with the system stability is revealed.

The rest of this paper is organized as follows. In Section II, the model of the DDWFV is developed. In Section III, the impact of system parameters on the SSO characteristics is analyzed, and in Section IV, the impact of the VSC-HVDC connection on the SSO is explored. In these cases, both the eigenvalue method and time-domain simulations are adopted. The SSO mechanisms are discussed in Section V. Concluding remarks are given in Section VI.
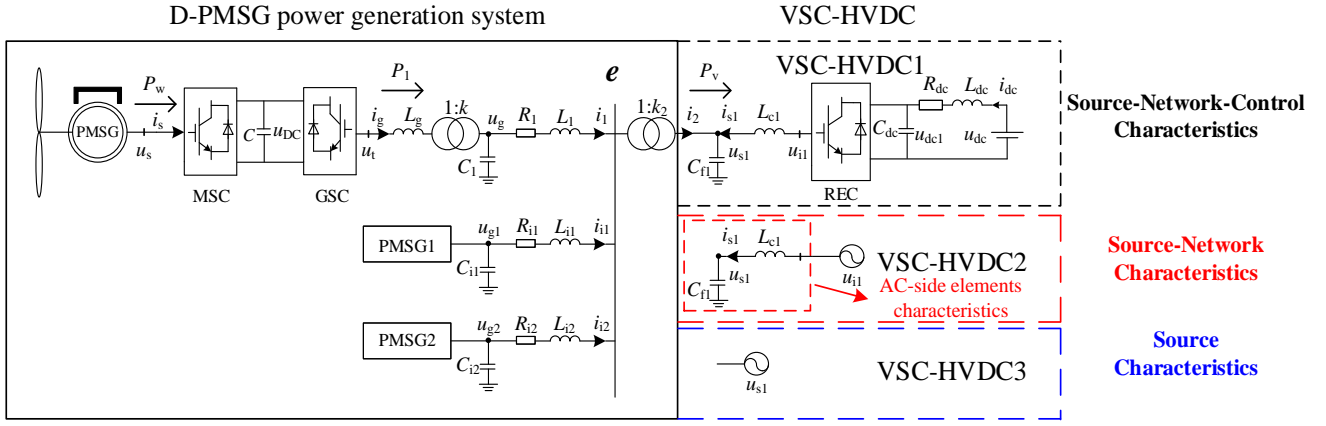
Fig. 1. System diagram of direct-drive wind farms interfaced with VSC-HVDC systems (MSC-machine-side converter, GSC-grid-side converter, REC-rectifier), where R_{i1}, L_{i1}, C_{i1} and R_{i2}, L_{i2}, C_{i2} are the resistance, inductance and capacitance of the AC transmission lines in the second and third wind farms.

II. MODELLING OF THE DDWFV

The diagram of the DDWFV is shown in Fig. 1. 40 wind turbines with the power rating of 5 MW for each are lumped into one unit of 200 MW capacity. Then, an equivalent model of a D-PMSG with the 200 MW installed capacity is equivalent to a direct-drive wind farm. In order to analyze the impact of the VSC-HVDC on the SSO characteristics, the DDWFV is divided into the D-PMSG power generation system and the VSC-HVDC, as shown in Fig. 1. The parameters of the D-PMSG power generation system are shown in Table A1 in Appendix, and the parameters of the VSC-HVDC are shown in Table A2 in Appendix.

A. Dynamic Model of the D-PMSG Power Generation System

Shaft model: The shaft system of the D-PMSG is modeled as a single-mass model as
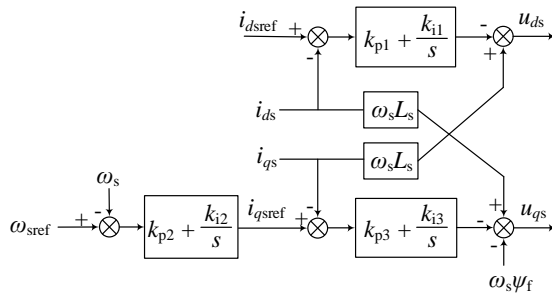
$$Jp\omega = T_M - T_e \tag{1}$$
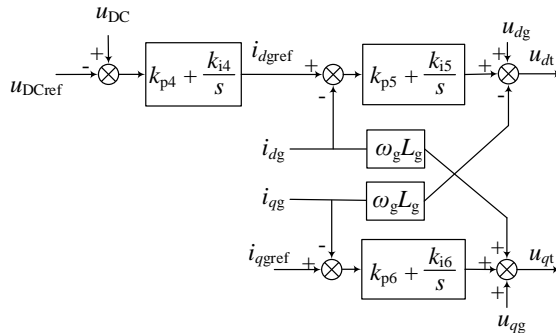

Fig. 2. Structure of the machine-side converter (MSC).

Fig. 3. Structure of the grid-side converter (GSC).

where $p = d/dt$; J is the total moment of inertia of the wind turbine generator (WTG); ω is the speed of the WTG; $T_M = 0.5\rho SC_p v^3/\omega$ with T_M being the mechanical torque of the WTG, ρ being the air density, S being the wind turbine sweeping area, C_p being the utilization coefficient of wind energy, and v being the wind speed; T_e is the electromagnetic torque of the generator, $T_e = 1.5n_p i_{qs}\psi_f$, in which n_p is the pole number of the permanent magnet motor, i_{qs} indicates the q-axis component of the stator current, and ψ_f represents the magnetic flux.

D-PMSG and back-to-back converter model: The dynamic models of the D-PMSG and back-to-back converter in the d- and q-frame are obtained as

$$\begin{cases} L_s p i_{ds} = u_{ds} - R_s i_{ds} + \omega_s L_s i_{qs} \\ L_s p i_{qs} = u_{qs} - R_s i_{qs} - \omega_s L_s i_{ds} - \omega_s \psi_f \\ Cu_{DC} p u_{DC} = 1.5(u_{ds} i_{ds} + u_{qs} i_{qs} - u_{dt} i_{dg} - u_{qt} i_{qg}) \end{cases} \tag{2}$$

in which L_s and R_s are the stator inductance and resistance, respectively. u_{ds}, u_{qs} and i_{ds}, i_{qs} are the d- and q- axis components of the stator voltage and current, and ω_s is the electric speed of the D-PMSG.

Back-to-back converter model: The machine-side converter (MSC) controls the d-axis current to be 0, which minimizes the loss of the generator. The DC voltage and reactive power are controlled by the GSC. The control structures of the MSC and GSC are shown in Figs. 2 and 3. The dynamic mathematical models of the MSC and GSC are shown as

$$\begin{cases} px_1 = i_{dsref} - i_{ds} \\ px_2 = \omega_{sref} - \omega_s \\ px_3 = i_{qsref} - i_{qs} \end{cases} \tag{3}$$

$$\begin{cases} px_4 = u_{DC} - u_{DCref} \\ px_5 = i_{dgref} - i_{dg} \\ px_6 = i_{qgref} - i_{qg} \end{cases} \tag{4}$$

PLL model of D-PMSG power generation system: The PLL control structure of the D-PMSG power generation system is shown in Fig. 4. In the GSC model of the D-PMSG, the d-q rotating coordinate system is set based on the node voltage u_g, and the q-axis component of u_g is the input of the PLL. The

dynamic mathematical model of the PLL in the D-PMSG power generation system is shown in (5).
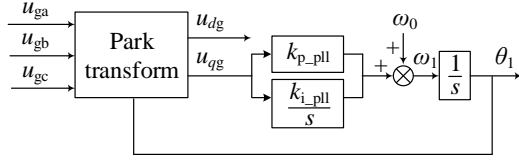

Fig. 4. Control structure of the PLL in the D-PMSG power generation system, where k_{p_pll} and k_{i_pll} are the proportional and integral coefficients in the PLL controller, respectively.

$$\begin{cases} px_{a1} = u_{qg} \\ px_{b1} = \omega_0 + k_{p\_pll}u_{qg} + k_{i\_pll}x_{a1} = \omega_1 \\ \theta_1 = x_{b1} \end{cases} \quad (5)$$

where $\omega_0 = 2\pi f_0$ is the reference frequency with $f_0 = 50$ Hz.

Wind power grid-connected transmission line model: The dynamic mathematical model of the wind power transmission line is shown as

$$\begin{cases} L_g pi_{dg} = u_{dt} - \dfrac{1}{k}u_{dg} + \omega_g L_g i_{qg} \\ L_g pi_{qg} = u_{qt} - \dfrac{1}{k}u_{qg} - \omega_g L_g i_{dg} \\ C_1 pu_{dg} = \dfrac{1}{k}i_{dg} - i_{d1} + \omega_g C_1 u_{qg} \\ C_1 pu_{qg} = \dfrac{1}{k}i_{qg} - i_{q1} - \omega_g C_1 u_{dg} \\ L_1 pi_{d1} = u_{dg} - R_1 i_{d1} - e_d + \omega_g L_1 i_{q1} \\ L_1 pi_{q1} = u_{qg} - R_1 i_{q1} - e_q - \omega_g L_1 i_{d1} \end{cases} \quad (6)$$

where ω_g is the angular frequency; u_{DC} is the DC-side voltage in the back-to-back converter; u_{dt}, u_{qt} and i_{dg}, i_{qg} are the d-axis and q-axis voltage and current of the GSC side, respectively; u_{dg} and u_{qg} are the d- and q-axis components of the voltage in the wind generator side; i_{d1} and i_{q1} are the d- and q-axis currents of the grid-connected transmission line, respectively; e_d and e_q are the d- and q-axis components of the point of common coupling (PCC) voltage in wind farms, respectively.

B. Dynamic Model of the VSC-HVDC System

In Fig. 1, the REC controls the AC voltage amplitude and frequency, and the inverter controls the DC voltage [25]. A constant DC voltage source is equivalent to the inverter station, which is shown as u_{dc} in Fig. 1. The control structure of the REC is shown in Fig. 5. The PLL of VSC-HVDC takes ω_0 as the input signal. The dynamic mathematical models of the AC system, the DC system and control system are given in (7)-(9).
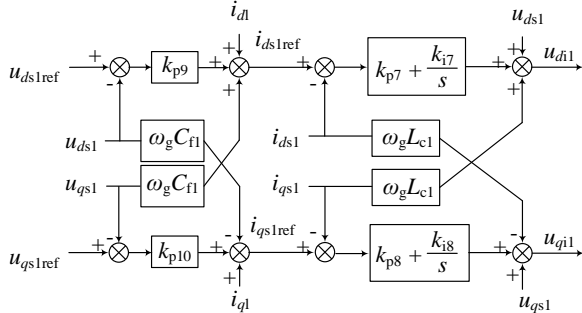

Fig. 5. Structure of the rectifier (REC).

$$\begin{cases} L_{c1} pi_{ds1} = \omega_g L_{c1} i_{qs1} + u_{di1} - u_{ds1} \\ L_{c1} pi_{qs1} = -\omega_g L_{c1} i_{ds1} + u_{qi1} - u_{qs1} \\ C_{f1} pu_{ds1} = i_{d2} + i_{ds1} + \omega_g C_{f1} u_{qs1} \\ C_{f1} pu_{qs1} = i_{q2} + i_{qs1} - \omega_g C_{f1} u_{ds1} \end{cases} \quad (7)$$

$$\begin{cases} L_{dc} pi_{dc} = u_{dc} - u_{dc1} - R_{dc} i_{dc} \\ C_{dc} u_{dc1} pu_{dc1} = u_{dc1} i_{dc} - \dfrac{3}{2}(u_{di1} i_{ds1} + u_{qi1} i_{qs1}) \end{cases} \quad (8)$$

$$\begin{cases} px_7 = i_{ds1ref} - i_{ds1} \\ px_8 = i_{qs1ref} - i_{qs1} \\ i_{ds1ref} = k_{p9}(u_{ds1ref} - u_{ds1}) + i_{d1} + \omega_g C_{f1} u_{qs1} \\ i_{qs1ref} = k_{p10}(u_{qs1ref} - u_{qs1}) + i_{q1} - \omega_g C_{f1} u_{ds1} \\ u_{di1} = u_{ds1} + \omega_g L_{c1} i_{qs1} + k_{p7}(i_{ds1ref} - i_{ds1}) + k_{i7} x_7 \\ u_{qi1} = u_{qs1} - \omega_g L_{c1} i_{ds1} + k_{p8}(i_{qs1ref} - i_{qs1}) + k_{i8} x_8 \end{cases} \quad (9)$$

C. System Small-Signal Model and Validation

According to the dynamic mathematical models of the above subsystems, the complete dynamic model of the DDWFV can be obtained. After linearization, the system small-signal model is expressed as

$$\frac{d\Delta x}{dt} = A\Delta x + B\Delta u \quad (10)$$

where Δx is the linearized state variable, Δu is the linearized input variable, A is the state matrix, and B is the input matrix. Each state variable and input variable are given as

$$\begin{cases} \Delta x = [\Delta\omega, \Delta i_{ds}, \Delta i_{qs}, \Delta u_{DC}, \Delta x_1, \Delta x_2, \Delta x_3, \Delta x_4, \Delta x_5, \Delta x_6, \\ \quad \Delta i_{dg}, \Delta i_{qg}, \Delta u_{dg}, \Delta u_{qg}, \Delta i_{d1}, \Delta i_{q1}, \Delta x_{a1}, \Delta x_{b1}, \Delta i_{ds1}, \Delta i_{qs1}, \\ \quad \Delta u_{ds1}, \Delta u_{qs1}, \Delta i_{dc}, \Delta u_{dc1}, \Delta x_7, \Delta x_8] \\ \Delta u = [\Delta i_{dsref}, \Delta\omega_{sref}, \Delta u_{DCref}, \Delta i_{qgref}, \Delta u_{ds1ref}, \Delta u_{qs1ref}] \end{cases} \quad (11)$$
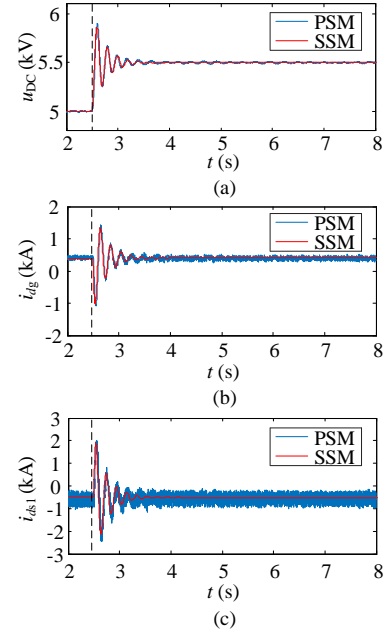

Fig. 6. System responses to a DC voltage step-change under the small-signal model and the PSCAD/EMTDC simulation model (SSM – small-signal model, PSM – PSCAD/EMTDC simulation model): (a) u_{DC} of the D-PMSG, (b) i_{dg} of the D-PMSG and (c) i_{ds1} of the VSC-HVDC.

Prior to analyzing the impact of system parameters on the SSO, the accuracy of the small-signal model (SSM) based on the MATLAB platform should be verified through time-domain simulations in PSCAD/EMTDC. The initial values of the DDWFV are given in Tables A1 and A2, except that the outer loop integral coefficient of the DC voltage controller is set to 133. The DDWFV is subject to a step change of u_{DCref} from 5 kV to 5.5 kV at 2.5 s. Fig. 6 shows the system responses under the SSM in MATLAB and the PSCAD/EMTDC simulation model (PSM). As it can be seen from Fig. 6, the responses of the SSM are consistent with those of the PSM, which confirms the accuracy of the developed SSM.

III. IMPACT OF SYSTEM PARAMETERS ON THE SSO CHARACTERISTICS

A. SSO Characteristics Analysis of a Single Direct-drive Wind Farm with the VSC-HVDC System

Based on the small-signal model of (10) and parameters in Tables A1 and A2 in Appendix, the eigenvalues of the single direct-drive wind farm interfaced with a VSC-HVDC system are calculated. The main oscillation modes of the system are shown in Table I.

TABLE I
OSCILLATION MODES OF A SINGLE DIRECT-DRIVE WIND FARM INTERFACED
WITH THE VSC-HVDC SYSTEM.

Oscillation modes	Eigenvalues	Oscillation frequency (Hz)	Damping ratio
$\lambda_{1,2}$	-31.650±j3651.4	581.14	0.0087
$\lambda_{3,4}$	-107.42±j1010.8	160.87	0.1057
$\lambda_{5,6}$	-78.116±j713.60	113.57	0.1088
$\lambda_{7,8}$	0.0223±j35.800	5.6978	-0.00062
$\lambda_{9,10}$	-54.178±j15.259	2.4285	0.9626

As it is listed in Table I, there are five oscillation modes in the system, including one SSO mode $\lambda_{7,8}$, one low-frequency oscillation mode $\lambda_{9,10}$ and the other three medium-frequency oscillation modes. The system presents negative damping to the

SSO mode $\lambda_{7,8}$ which greatly impacts the system stability, and the normalized participation factors of the SSO mode $\lambda_{7,8}$ are shown in Fig. 7.
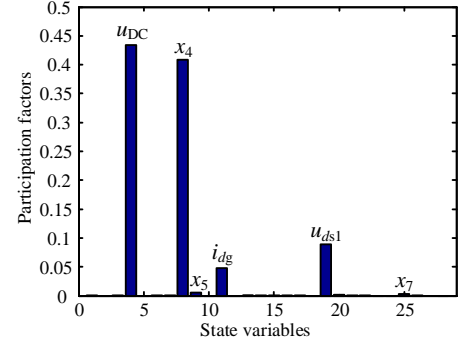

Fig. 7. Normalized participation factors of the SSO mode $\lambda_{7,8}$.

It can be seen from Fig. 7 that the state variables related to the SSO mode $\lambda_{7,8}$ are u_{DC}, x_4, x_5, i_{dg} in the D-PMSG power generation system and u_{ds1}, x_7 in the VSC-HVDC system. It is further found from (4) and (9) that x_4 and x_5 belong to the DC voltage controller of the D-PMSG power generation system, and x_7 belongs to the d-axis voltage controller of the VSC-HVDC. Thus, the SSO mode is mainly related to the GSC controller of the D-PMSG power generation system and the REC controller of the VSC-HVDC as well as the relevant system parameters. As the impact of controller parameters on the SSO characteristics has been analyzed in [25]-[41], this paper focuses on the influence of system parameters on the damping and frequency characteristics of the SSO mode.

Considering that the remaining system parameters are unchanged, the change of the relevant system parameters affects the SSO, as shown in Fig. 8. Here, the DC-side capacitor C (16-406 mF) of the D-PMSG power generation system, the DC-side capacitor C_{dc} (150-600 µF) and reactance L_{dc} (0.1 mH-0.01 H) of the VSC-HVDC, the VSC-HVDC AC-side phase reactor L_{c1} (1-15 mH), the X/R ratio (31.7956-0.3527)
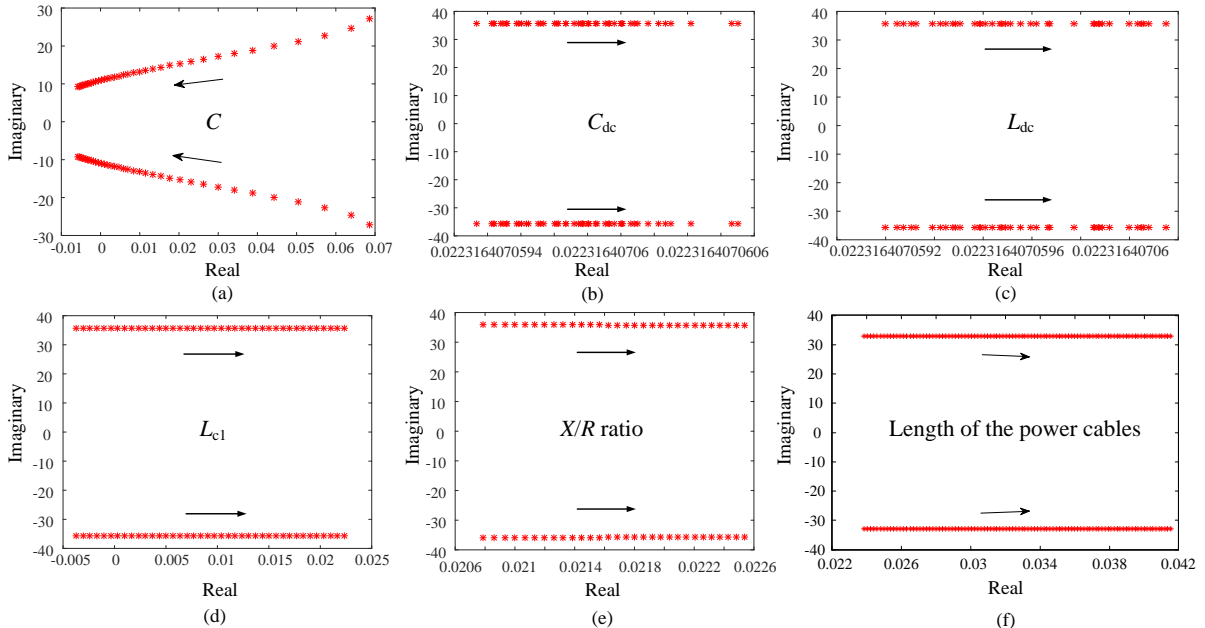

Fig. 8. Variation of the SSO eigenvalue with the change of system parameters: (a) DC-side capacitor C of back-to-back converter, (b) DC-side capacitor C_{dc} of VSC-HVDC, (c) DC-side inductor L_{dc} of VSC-HVDC, (d) phase inductor L_{c1} of VSC-HVDC, (e) X/R ratio of the collector cable impedance and (f) length of the power cables.

and the length of the power cables (1 km-5 km, $r_1 = 0.05$ Ω/km, $l_1 = 0.001$ H/km, $c_1 = 5$ μF/km) vary. The impact of system parameters on the damping characteristics and frequency characteristics of the SSO mode is obtained according to Fig. 8, as shown in Table II.

TABLE II
THE IMPACT OF SYSTEM PARAMETERS ON THE DAMPING CHARACTERISTICS AND FREQUENCY CHARACTERISTICS OF THE SSO MODE

Parameters	Damping	Frequency
C ↑	↑	↓
C_{dc} ↑	-	-
L_{dc} ↑	-	-
L_{c1} ↑	↓	-
X/R ratio ↑	↓	-
Length of the power cables ↑	↓	-

Notes: ↑ denotes increase; ↓ denotes decrease; - denotes unchanging.

Table II shows that for the eigenvalue analysis in the DC system, when C increases, the SSO damping is enhanced and the frequency decreases. This means that the system gradually becomes stable. Furthermore, C_{dc} and L_{dc} have negligible impact on the SSO. For eigenvalue analysis in the AC system, the increase of L_{c1} leads to a decrease of the SSO damping, and the system gradually becomes unstable. However, in this case, the frequency remains unchanged. With the increase of the length of the power cables, the SSO damping decreases, whereas the frequency remains unchanged. Therefore, for renewable-based intermittent sources like wind, the generators should be connected to the VSC-HVDC through short-distance collector cables. Additionally, when the X/R ratio of the power cable impedance increases, the SSO damping is weakened while the SSO frequency is almost not changed. Generally, the X/R ratio of the high-voltage collector cable impedance is high, whereas the X/R ratio of the low-voltage collector cable impedance is low [44]. Considering the X/R characteristics of the collector cable impedance, the SSO is more likely to occur when the D-PMSG power generation system is connected to the VSC-HVDC through high-voltage collector cables. However, the voltage level of the collector cables also affects the equivalent impedance, which in the high-voltage transmission side is less than that in the low-voltage transmission side, and small equivalent impedances improve the SSO stability. Thus, it is difficult to reach a general conclusion of the impact of the collector cable voltage level on the SSO characteristics.

It is worth mentioning that the eigenvalue analysis in Table II assumes that the inverter of VSC-HVDC is simply replaced with a DC voltage source. Normally, when the onshore AC power grid is strong and C_{dc} is large, the DC voltage controller dynamics of the inverter have a negligible impact on the AC-side dynamics of the REC [27]. Then, the inverter station can be replaced with a DC voltage source to simulate the effect of the DC voltage controller. However, when the assumption is not satisfied, the DC voltage controller of the VSC-HVDC may affect the SSO to a large extent. Then, the eigenvalue analysis results in Table II should be reevaluated considering the dynamic characteristics of the inverter station.

B. Time-domain Simulation

To verify the above analysis, referring to Fig. 1, a single direct-drive wind farm with a VSC-HVDC system is built in PSCAD/EMTDC. Since the changes of C, L_{c1}, X/R ratio and the length of the power cables affect the system stability significantly, those parameters are changed at 5.0 s, whereas the other parameters remain unchanged. The simulation results of i_{dg} are shown in Fig. 9.
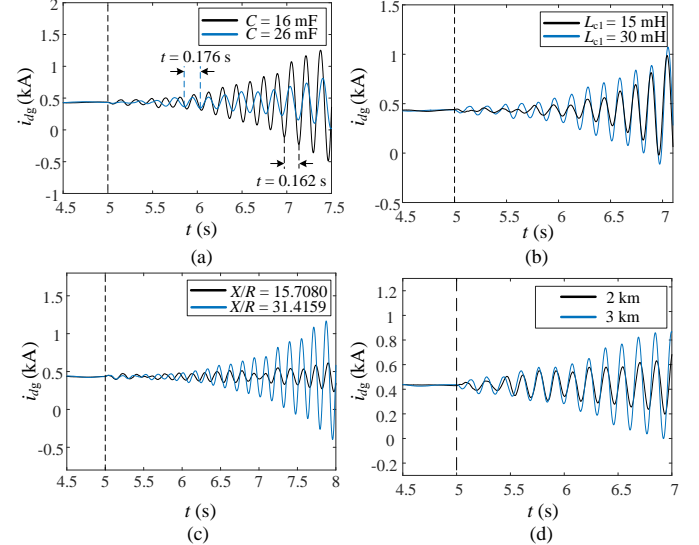

Fig. 9. Simulation results (i_{dg}) of the single direct-drive wind farm with a VSC-HVDC system with the change of system parameters: (a) the impact of C, (b) the impact of L_{c1}, (c) the impact of X/R ratio and (d) the impact of the length of the power cables.

As observed in Fig. 9(a), when $C = 26$ mF, the SSO damping is more effective than the damping when $C = 16$ mF. At the same time, the SSO frequency when $C = 26$ mF is 5.6818 Hz (oscillation period is 0.176 s), and the SSO frequency is less than 6.1728 Hz when $C = 16$ mF (oscillation period is 0.162 s). The impact of C on the SSO characteristics in Fig. 9(a) verifies the eigenvalue analysis of Fig. 8(a). In addition, Figs. 9(b)-(d) show that the SSO damping is weaker with the increase of L_{c1}, X/R ratio and the length of the power cables while the SSO frequency is almost not changed, which verifies the eigenvalue analysis presented in Figs. 8(d)-(f).

According to the above discussions, with the increase of C and the decrease of L_{c1}, X/R ratio and the length of the power cables, the SSO stability is improved. The system parameters are the inherent characteristics of the DDWFV and cannot change dynamically. Thus, the analysis in this section mainly aims to guide the system parameter design in the planning phase. That is, for engineers and consultants responsible for the design and planning phases of the DDWFV, several mitigation measures should be taken to avoid the SSO:

1) The D-PMSG power generation system should be connected to the VSC-HVDC through short-distance collector cables with a low X/R ratio.
2) In the planning phase of the DDWFV, a large DC capacitance of the D-PMSG should be designed, while the phase reactor of the VSC-HVDC should be small.

To verify the mitigation measures, further simulations of the interconnected system are performed and the parameters of the system are listed in Tables A1 and A2 in Appendix. The outer loop integral coefficient of the DC voltage controller is set to 133. Figs. 10(a)-(d) show the responses of the output active power at PCC under a 20%-rated power condition, when a three-phase ground fault happens in the common bus at $t = 5$ s

and it is cleared after 50 ms. According to Fig. 10, with the increase of C and the decrease of L_{c1}, X/R ratio and the lengths of the power cables, the SSO is mitigated.

As concluded in [38], [45], a simple aggregation of the wind farm resulted in certain misleading conclusions in wind farms with VSC-HVDC systems. To analyze the adequacy of the analysis in Fig. 8 for a multi-machine wind farm with VSC-HVDC systems, a two-machine D-PMSG-based wind farm with a VSC-HVDC system is built in PSCAD/EMTDC according to Fig. 1. The entire wind farm is modelled by two equivalent WTGs with 100 MW capacity for each. Based on the parameters in Tables A1 and A2 in Appendix, with the change of different system parameters, the waveforms of the output active power in the D-PMSGs and the VSC-HVDC under a 20%-rated power condition are shown in Fig. 11.

As it is observed in Fig. 11, with the increase of C and the decrease of L_{c1}, X/R ratio and the length of the power cables, the SSO stability of the two-machine D-PMSG-based wind farm with a VSC-HVDC system is improved. This conclusion is the same as that of Fig. 8 in the single-machine D-PMSG-based wind farm with a VSC-HVDC system. Thus, the aggregation does not affect the sensitivity analysis of system parameters. However, it can be seen from Fig. 11(a) that the SSO frequency of the output active power in the D-PMSGs is not the same as that in the VSC-HVDC. This implies that one more SSO mode may appear due to the interactions among multiple WTGs [17], [45].

IV. IMPACT OF THE VSC-HVDC CONNECTION ON THE SSO CHARACTERISTICS

In order to analyze the impact of the VSC-HVDC connection on the SSO characteristics, the VSC-HVDC system is divided into three parts: source, network and control, as shown in Fig. 1. The source characteristics include the AC-side controlled voltage source and the DC-side controlled current source. The network characteristics include the AC-side and the DC-side networks, and the control characteristic is represented by the REC controller. According to Figs. 8(b) and (c), the DC-side elements characteristics have negligible impact on the system stability. Thus, this section focuses on the impact of the control and AC-side elements characteristics. The source and source-network characteristics of the VSC-HVDC are shown in Fig. 1 without considering the DC-side elements. To facilitate the subsequent analysis, VSC-HVDC1, VSC-HVDC2 and VSC-HVDC3 are defined as

1)VSC-HVDC1: VSC-HVDC source-network-control system.
2)VSC-HVDC2: VSC-HVDC source-network system.
3)VSC-HVDC3: VSC-HVDC source system.

Accordingly, the SSO characteristic analysis in Section III is considered as the SSO analysis in the case of direct-drive wind farms with the VSC-HVDC1 system.

A. Impact of Control Characteristics

To investigate the impact of control characteristics on the system stability, the stability analysis of the direct-drive wind farms with the divided VSC-HVDC1 and VSC-HVDC2 should be compared. The small-signal model of the direct-drive wind farms with the VSC-HVDC2 system is established, and the state variable x_n and the input variable u_1 are shown in (12).
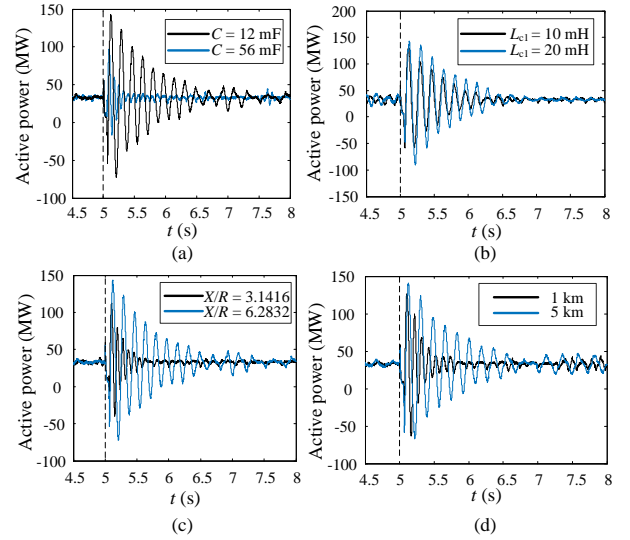
Fig. 10. Output active power of wind farms at the point of common coupling with the change of system parameters: (a) the impact of C, (b) the impact of L_{c1}, (c) the impact of X/R ratio and (d) the impact of the length of the power cables.

Fig. 11. Simulation results (the output active power P_1, P_2 in the grid-side of the first and second D-PMSGs and the output active power P_v in the VSC-HVDC) of the two-machine D-PMSG-based wind farm with a VSC-HVDC system with the change of system parameters: (a) the impact of C, (b) the impact of L_{c1}, (c) the impact of X/R ratio and (d) the impact of the length of the power cables.

$$\begin{cases}\Delta\boldsymbol{x}_{\mathrm{n}} = [\Delta\omega, \Delta i_{ds}, \Delta i_{qs}, \Delta u_{\mathrm{DC}}, \Delta x_1, \Delta x_2, \Delta x_3, \Delta x_4, \Delta x_5, \Delta x_6, \Delta x_{a1}, \\ \quad \Delta x_{b1}, \Delta i_{dg}, \Delta i_{qg}, \Delta u_{dg}, \Delta u_{qg}, \Delta i_{d1}, \Delta i_{q1}, \Delta i_{ds1}, \Delta i_{qs1}, \Delta u_{ds1}, \Delta u_{qs1}] \\ \Delta\boldsymbol{u}_1 = [\Delta i_{ds\mathrm{ref}}, \Delta\omega_{s\mathrm{ref}}, \Delta u_{\mathrm{DCref}}, \Delta i_{qg\mathrm{ref}}]\end{cases} \quad (12)$$

The eigenvalue analysis results of the direct-drive wind farms with the VSC-HVDC2 system are shown in Table III. Comparing Table I and Table III, the SSO damping ratio changes from -0.00062 to -0.0053, and the SSO frequency is almost unchanged. Thus, the control characteristics of the VSC-HVDC increase the SSO damping.

B. Impact of AC-side Characteristics

To explore the impact of AC-side elements characteristics on the SSO, the stability analysis of direct-drive wind farms with the divided VSC-HVDC2 and VSC-HVDC3 is compared. Similarly, the small-signal model of direct-drive wind farms with the VSC-HVDC3 system is established, and the state variable $\boldsymbol{x}_s$ and the input variable $\boldsymbol{u}_2$ are shown as
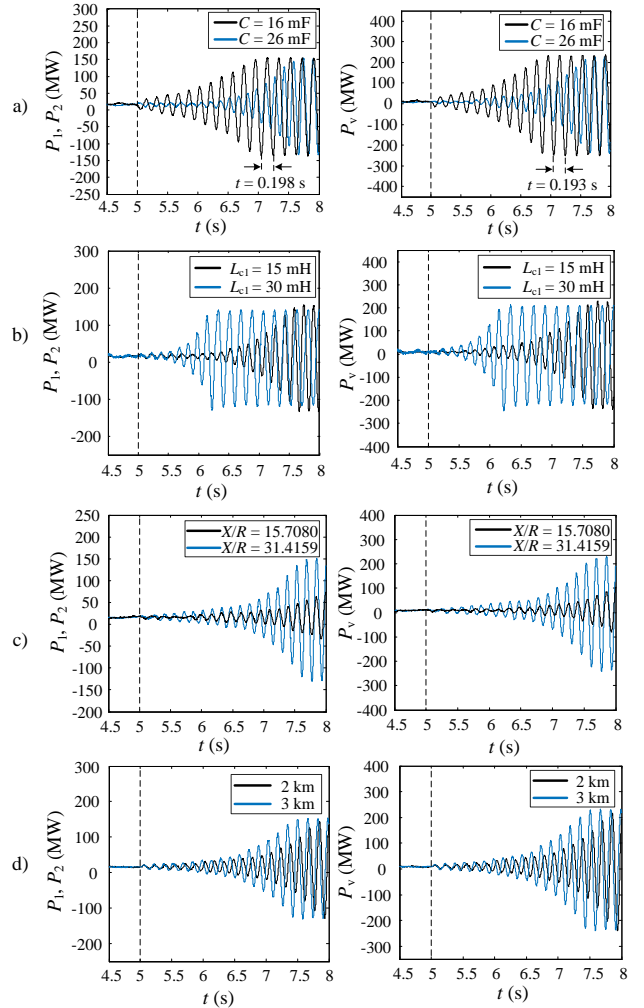
$$\begin{cases}\Delta\boldsymbol{x}_{\mathrm{s}} = [\Delta\omega, \Delta i_{ds}, \Delta i_{qs}, \Delta u_{\mathrm{DC}}, \Delta x_1, \Delta x_2, \Delta x_3, \Delta x_4, \Delta x_5, \\ \quad \Delta x_6, \Delta x_{a1}, \Delta x_{b1}, \Delta i_{dg}, \Delta i_{qg}, \Delta u_{dg}, \Delta u_{qg}, \Delta i_{d1}, \Delta i_{q1}] \\ \Delta\boldsymbol{u}_2 = [\Delta i_{ds\mathrm{ref}}, \Delta\omega_{s\mathrm{ref}}, \Delta u_{\mathrm{DCref}}, \Delta i_{qg\mathrm{ref}}]\end{cases} \quad (13)$$

The eigenvalue analysis results of the direct-drive wind farms with the VSC-HVDC3 system are shown in Table IV. By comparing Table III and Table IV, the SSO damping ratio changes from -0.0053 to -0.0015, and the SSO frequency is almost not changed. This indicates that the AC-side elements characteristics of the VSC-HVDC decrease the SSO damping.

TABLE III
OSCILLATION MODES OF DIRECT-DRIVE WIND FARMS INTERFACED WITH THE VSC-HVDC2 SYSTEM.

Oscillation modes	Eigenvalues	Oscillation frequency (Hz)	Damping ratio
$\lambda_{1,2}$	-33.393±j1569.0	249.71	0.0213
$\lambda_{3,4}$	-33.415±j901.29	143.44	0.0370
$\lambda_{5,6}$	0.1870±j35.234	5.6077	-0.0053

TABLE IV
OSCILLATION MODES OF DIRECT-DRIVE WIND FARMS INTERFACED WITH THE VSC-HVDC3 SYSTEM.

Oscillation mode	Eigenvalue	Oscillation frequency (Hz)	Damping ratio
$\lambda_{1,2}$	0.0545±j35.470	5.6452	-0.0015

C. Time-domain Simulation

To verify the impact of the control characteristics and AC-side elements characteristics of the VSC-HVDC on the system stability, the simulation models of the direct-drive wind farms interfaced with the VSC-HVDC1, VSC-HVDC2 and VSC- HVDC3 are built in PSCAD/EMTDC according to Fig. 1. In the three scenarios, the DC-side capacitance C changes from 300 mF to 20 mF at 4.0 s. The simulation results (i_{dg}) of the system are shown in Fig. 12.

As it is observed in Fig. 12, when C changes from 300 mF to 20 mF at 4.0 s, the SSO appears in i_{dg} for all the three cases. When the controller enters the limiting area, i_{dg} is capped with the limit. Meanwhile, it is shown in Fig. 12 that the SSO frequencies in the three scenarios are close, which is in agreement with the SSO frequency analysis results in Tables I, III and IV. Additionally, Fig. 12 shows that the fastest

divergence occurs when the D-PMSG wind farm is connected to the VSC-HVDC2, and the second fastest divergence occurs when it is connected to the VSC-HVDC3. In contrast, the lowest divergence occurs when it is connected to the VSC-HVDC1. Hence, the control characteristics of the VSC-HVDC increase the SSO damping effect, while the AC-side elements characteristics reduce it. In summary, the time-domain simulation results are in accordance with the SSO damping analysis in Tables I, III and IV. As the control characteristics provide a positive damping effect and the AC-side elements characteristics provide a negative one, whether the VSC-HVDC connection contributes to the system stability is decided by the two factors and should be analyzed with respect to specific scenarios.
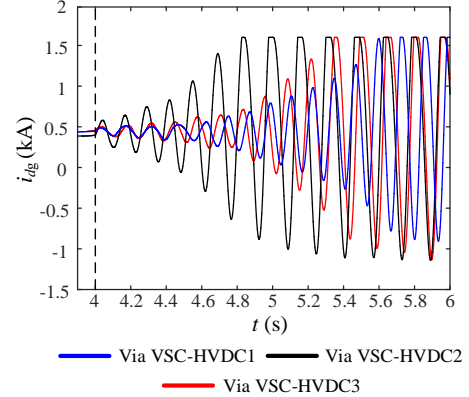
Fig. 12. Simulation results (i_{dg}) of the system under three different scenarios.

V. SSO MECHANISM ANALYSIS OF THE INTERCONNECTED SYSTEM

A. SSO Mechanism Analysis

With the eigenvalue analysis, the oscillation modes and the normalized participation factors of the SSO mode can be obtained. However, this cannot give a detailed explanation of the SSO process. Moreover, the impedance analysis and open-loop modal method only reflect the interaction process between two subsystems, while the dynamic process within the subsystem cannot be reflected in detail. To provide new insights into the SSO mechanism, the interactions among relevant state variables are discussed in the following, which reveals the dynamic process of the entire system, including the dynamic interactions within the subsystem. Firstly, the state variables and controllers related to SSO modes are determined by the participation factor analysis, and then the linearized relationship among these variables is deduced. Subsequently, the interactions among the relevant state variables are obtained considering the influence of the linearized equation relationship and relevant controllers. Finally, the instability mechanism is revealed.

1) *Determination of state variables and controllers:* It can be known from Fig. 7 that the SSO mode is affected by u_{DC}, x_4, x_5 (i.e., $x_4 = \int(u_{\mathrm{DC}} - u_{\mathrm{DCref}})\mathrm{d}t$, $x_5 = \int(i_{dg\mathrm{ref}} - i_{dg})\mathrm{d}t$), i_{dg} in the D-PMSG power generation system and u_{ds1}, x_7 (i.e., $x_7 = \int(i_{ds1\mathrm{ref}} - i_{ds1})\mathrm{d}t$) in the VSC-HVDC system. Therefore, both the DC voltage controller of direct-drive wind farms and the d-axis AC voltage controller of the VSC-HVDC have a significant effect on the SSO mode.
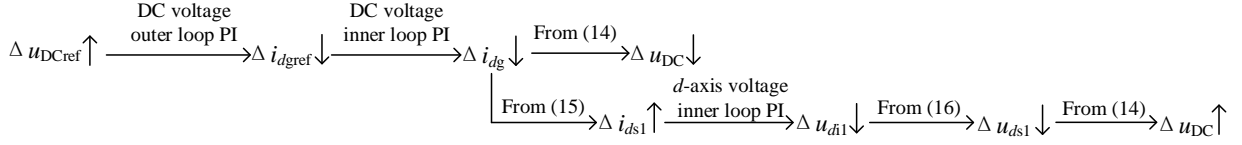
Fig. 13. Entire response of the interactions among relevant state variables under the disturbance of u_{DCref}.

2) Linearized relationship among the relevant state variables:
To analyze the interactions among the state variables, the linearized relationship should be deduced. After the derivation, the linearized relationship among u_{DC}, u_{ds1} and i_{dg} is shown as

$$Cu_{DC0}\frac{du_{DC}}{dt}+\frac{2P_{w0}+3u_{dt0}i_{dg0}}{2u_{DC0}}\Delta u_{DC}$$
$$=1.5[-\frac{i_{dg0}}{kk_2}\Delta u_{ds1}+(\frac{i_{dg0}R_1}{k^2}+u_{dt0})\Delta i_{dg}] \quad (14)$$

where P_w is the output active power of the D-PMSG, as shown in Fig. 1, and the variables with the subscript "0" are the steady-state operating points after the linearization. The linearized relationship between i_{dg} and i_{ds1} is obtained when the currents in the capacitors (C_1 and C_{f1}) are neglected as

$$\Delta i_{dg}=-kk_2\Delta i_{ds1} \quad (15)$$

Notably, as C_1 and C_{f1} are relatively small, the currents through them are neglected. Meanwhile, the linearized relationship among u_{ds1}, u_{di1} and i_{ds1} is obtained as

$$\Delta u_{ds1}=\Delta u_{di1}+\omega_g L_{c1}\Delta i_{qs1}-L_{c1}\frac{d\Delta i_{ds1}}{dt} \quad (16)$$

3) Interactions among the relevant state variables:
When the D-PMSG power generation system should increase the DC voltage, the DC voltage controller of the GSC will increase the outer loop DC voltage reference u_{DCref}. The entire response of the state variables in this case is shown in Fig. 13. The entire response is comprised of a positive feedback system and a negative feedback system as follows:

3.1) *Positive feedback system:* With the increase of u_{DCref}, the output current reference i_{dgref} will decrease due to the DC voltage outer-loop PI controller. This thus makes the output current i_{dg} decrease due to the regulation from the DC voltage inner-loop PI controller. From (14), it is known that a decrease of i_{dg} results in a decrease of u_{DC}, which in turn leads to a further decrease of i_{dg} due to the DC voltage outer-loop controller, and eventually leading to a smaller DC voltage or even system instability. The detailed interactive process is a positive feedback system, as shown in Fig. 14.
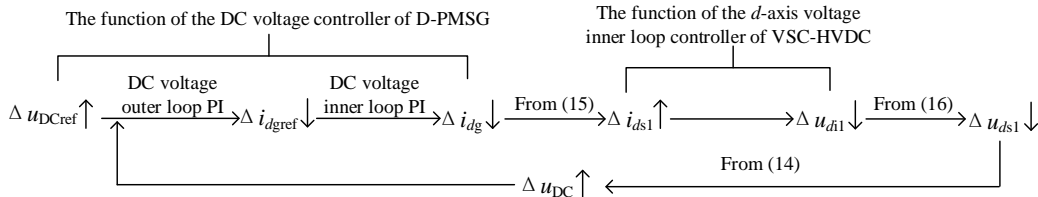

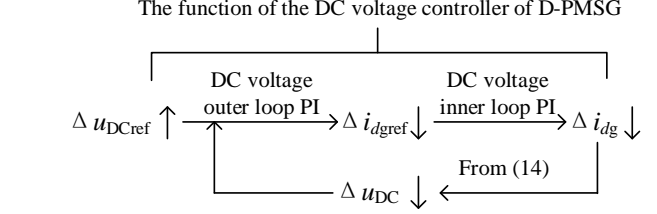Fig. 14. Positive feedback system in the entire response.

3.2) *Negative feedback system:* Meanwhile, according to (15), the decrease of i_{dg} results in an increase of i_{ds1}, and then the decrease of u_{di1} under the impact of the *d*-axis voltage inner-loop PI controller of the REC. Following (16), it is known that u_{ds1} will decrease, and then from (14), u_{DC} will increase, which mitigates the adverse impact of the positive feedback system as discussed previously. That is, the interactive process is a negative feedback system, as shown in Fig. 15.

The above analysis shows that the positive feedback loop in Fig. 14 results in instability, and this loop is mainly affected by the DC voltage controller in the D-PMSG power generation system. Meanwhile, the negative feedback loop in Fig. 15 mitigates the adverse effect of the positive feedback loop, and this loop is mainly affected by the DC voltage controller in the D-PMSG power generation system and *d*-axis voltage controller of the REC in the VSC-HVDC system. As both the positive feedback system and negative feedback system are affected by the DC voltage controller of the D-PMSG, the impact of the DC voltage controller parameters on the overall system is difficult to analyze from Fig. 13. However, the *d*-axis voltage inner-loop controller of the VSC-HVDC only affects the negative feedback system. The larger the coefficients of the negative feedback are, the stronger effect the negative feedback has on the system stability. As a result, the larger the coefficients of the *d*-axis voltage inner-loop controller are, the more stable the interconnected system is.

To theoretically explain the positive feedback system and negative feedback system, the control block diagrams of the two feedbacks are presented in Fig. 16. According to Fig. 16, the closed-loop transfer function $G_p(s)$ of the positive feedback is obtained, as shown in (17). The closed-loop transfer function $G_n(s)$ of the negative feedback is also calculated, as shown in
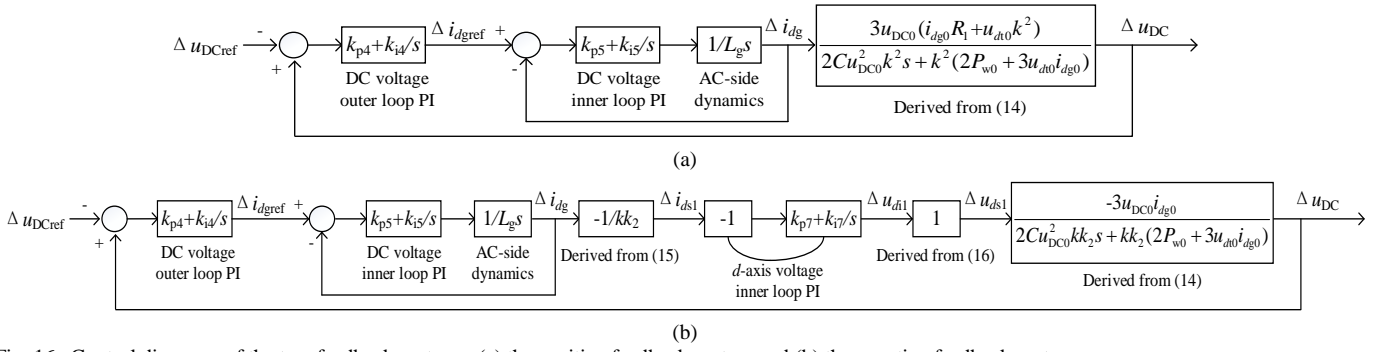

Fig. 15. Negative feedback system in the entire response.

Fig. 16. Control diagrams of the two feedback systems: (a) the positive feedback system and (b) the negative feedback system.

$$G_{\mathrm{p}}(s) = \frac{\Delta u_{\mathrm{DC}}}{\Delta u_{\mathrm{DCref}}} = \frac{G_{\mathrm{p1}}(s)}{G_{\mathrm{p1}}(s)-1}, \; G_{\mathrm{p1}}(s) = (k_{\mathrm{p4}} + \frac{k_{\mathrm{i4}}}{s})\frac{G_{\mathrm{p2}}(s)}{1+G_{\mathrm{p2}}(s)}\frac{3u_{\mathrm{DC0}}(i_{dg0}R_1 + u_{dt0}k^2)}{2Cu_{\mathrm{DC0}}^2 k^2 s + k^2(2P_{\mathrm{w0}} + 3u_{dt0}i_{dg0})}, \; G_{\mathrm{p2}}(s) = (k_{\mathrm{p5}} + \frac{k_{\mathrm{i5}}}{s})\frac{1}{L_{\mathrm{g}}s} \quad (17)$$

$$G_{\mathrm{n}}(s) = \frac{\Delta u_{\mathrm{DC}}}{\Delta u_{\mathrm{DCref}}} = \frac{G_{\mathrm{n1}}(s)}{G_{\mathrm{n1}}(s)-1}, \; G_{\mathrm{n1}}(s) = -(k_{\mathrm{p4}} + \frac{k_{\mathrm{i4}}}{s})(k_{\mathrm{p7}} + \frac{k_{\mathrm{i7}}}{s})\frac{G_{\mathrm{p2}}(s)}{1+G_{\mathrm{p2}}(s)}\frac{1}{kk_2}\frac{3u_{\mathrm{DC0}}i_{dg0}}{2Cu_{\mathrm{DC0}}^2 kk_2 s + kk_2(2P_{\mathrm{w0}} + 3u_{dt0}i_{dg0})} \quad (18)$$

(18). To analyze the stability of the two feedback systems, the characteristic equations of (17) and (18) are derived, as shown in (19) and (20), respectively. Applying the Routh's stability criterion, as the coefficients of (19) are not all positive, a root or multiple roots exist, which are imaginary or have positive real parts [46]. In this case, the positive feedback system shown in Fig. 14 is unstable, and the positive root is calculated to be 1.072 based on the values in Tables A1 and A2. Meanwhile, the roots of (20) are obtained: $s_{\mathrm{n1}} = -1.814$, $s_{\mathrm{n2}} = -0.054 \pm j0.075$, $s_{\mathrm{n3}} = -0.054 \pm j0.008$. Thus, the negative feedback system shown in Fig. 15 is stable.

$$\begin{cases} a_{\mathrm{p4}}s_{\mathrm{p}}^4 + a_{\mathrm{p3}}s_{\mathrm{p}}^3 + a_{\mathrm{p2}}s_{\mathrm{p}}^2 + a_{\mathrm{p1}}s_{\mathrm{p}} + a_{\mathrm{p0}} = 0 \\ a_{\mathrm{p4}} = -2Cu_{\mathrm{DC0}}^2 k^2 L_{\mathrm{g}} \\ a_{\mathrm{p3}} = -2Ck_{\mathrm{p5}}u_{\mathrm{DC0}}^2 k^2 - L_{\mathrm{g}}k^2(2P_{\mathrm{w0}} + 3u_{dt0}i_{dg0}) \\ a_{\mathrm{p2}} = -2Ck_{\mathrm{i5}}u_{\mathrm{DC0}}^2 k^2 - k_{\mathrm{p5}}k^2(2P_{\mathrm{w0}} + 3u_{dt0}i_{dg0}) + 3u_{\mathrm{DC0}}k_{\mathrm{p4}}k_{\mathrm{p5}}(i_{dg0}R_1 + k^2 u_{dt0}) \\ a_{\mathrm{p1}} = -k_{\mathrm{i5}}k^2(2P_{\mathrm{w0}} + 3u_{dt0}i_{dg0}) + 3u_{\mathrm{DC0}}(k_{\mathrm{i4}}k_{\mathrm{p5}} + k_{\mathrm{p4}}k_{\mathrm{i5}})(i_{dg0}R_1 + k^2 u_{dt0}) \\ a_{\mathrm{p0}} = 3u_{\mathrm{DC0}}k_{\mathrm{i4}}k_{\mathrm{i5}}(i_{dg0}R_1 + k^2 u_{dt0}) \end{cases}$$

$$(19)$$

$$\begin{cases} a_{\mathrm{n5}}s_{\mathrm{n}}^5 + a_{\mathrm{n4}}s_{\mathrm{n}}^4 + a_{\mathrm{n3}}s_{\mathrm{n}}^3 + a_{\mathrm{n2}}s_{\mathrm{n}}^2 + a_{\mathrm{n1}}s_{\mathrm{n}} + a_{\mathrm{n0}} = 0 \\ a_{\mathrm{n5}} = 2CL_{\mathrm{g}}(u_{\mathrm{DC0}}kk_2)^2 \\ a_{\mathrm{n4}} = 2Ck_{\mathrm{p5}}(u_{\mathrm{DC0}}kk_2)^2 + L_{\mathrm{g}}(kk_2)^2(2P_{\mathrm{w0}} + 3u_{dt0}i_{dg0}) \\ a_{\mathrm{n3}} = 2Ck_{\mathrm{i5}}(u_{\mathrm{DC0}}kk_2)^2 + k_{\mathrm{p5}}(kk_2)^2(2P_{\mathrm{w0}} + 3u_{dt0}i_{dg0}) + 3u_{\mathrm{DC0}}i_{dg0}k_{\mathrm{p4}}k_{\mathrm{p5}}k_{\mathrm{p7}} \\ a_{\mathrm{n2}} = k_{\mathrm{i5}}(kk_2)^2(2P_{\mathrm{w0}} + 3u_{dt0}i_{dg0}) + 3u_{\mathrm{DC0}}i_{dg0}[k_{\mathrm{p7}}(k_{\mathrm{p4}}k_{\mathrm{i5}} + k_{\mathrm{i4}}k_{\mathrm{p5}}) + k_{\mathrm{p4}}k_{\mathrm{p5}}k_{\mathrm{i7}}] \\ a_{\mathrm{n1}} = 3u_{\mathrm{DC0}}i_{dg0}[k_{\mathrm{i7}}(k_{\mathrm{p4}}k_{\mathrm{i5}} + k_{\mathrm{i4}}k_{\mathrm{p5}}) + k_{\mathrm{p7}}k_{\mathrm{i4}}k_{\mathrm{i5}}] \\ a_{\mathrm{n0}} = 3u_{\mathrm{DC0}}i_{dg0}k_{\mathrm{i4}}k_{\mathrm{i5}}k_{\mathrm{i7}} \end{cases}$$

$$(20)$$

As it can be known from (19) and (20), the coefficients k_{p4}, k_{p5}, k_{i4}, k_{i5} of the DC voltage controller in the D-PMSG power generation system affect the two feedback systems at the same time. Therefore, it is difficult to analyze the impact of the DC voltage controller parameters on the overall system from (19) and (20). However, the d-axis voltage controller of the VSC-HVDC only affects the negative feedback system. The dominant root locus of the negative feedback system with the

change of the parameters in the d-axis voltage controller is obtained, as shown in Fig. 17. It is observed in Fig. 17 that with the increase of k_{p7} and k_{i7}, the dominant root moves to the left, which implies that the system becomes more stable. Therefore, the theoretical analysis verifies that the larger the coefficients of the d-axis voltage inner-loop controller are, the larger the gain of the negative feedback will be and the stronger effect the negative feedback will have on the system stability.
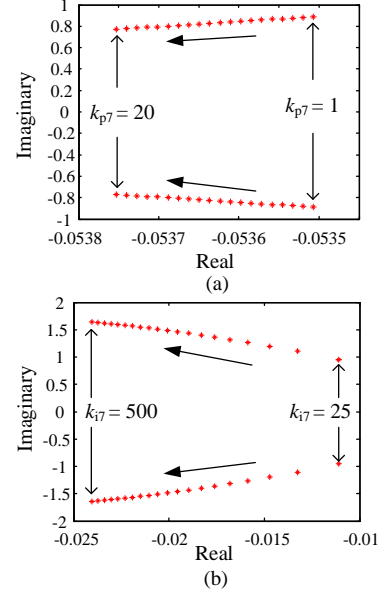

Fig. 17. Dominant root locus of the negative feedback system with the change of k_{p7} and k_{i7}: (a) k_{p7} and (b) k_{i7}.

B. Time-domain Simulation

In brief, with the increase of the gain of the negative feedback, the SSO is mitigated. To verify the mitigation method, a time-domain simulation model of the interconnected system is built. The simulation parameters of the system are listed in Tables A1 and A2 in Appendix, and the outer loop integral coefficient of the DC voltage controller is set to 133. Fig. 18 shows the responses of i_{dg} with different k_{p7} and k_{i7}, when a three-phase ground fault happens in the common bus at $t = 5$ s and it is cleared after 50 ms. It can be observed from Fig. 18 that with the increase of k_{p7} and k_{i7}, the SSO is mitigated.

This implies that with the increase of the gain of the negative feedback system, the SSO stability is improved. In summary, the time-domain simulation results of Fig. 18 are in accordance with the SSO mechanism analysis of Figs. 13 and 17. Compared with the eigenvalue analysis method, the SSO mechanism analysis in this section provides a physical explanation for the SSO from the perspective of the positive feedback system and negative feedback system. In addition, compared with the impedance analysis method and open-loop modal method, instead of simplifying the subsystems into impedances or eigenvalues, the dynamic interactions within the subsystems are revealed by exploring the dynamic interactions among relevant state variables.
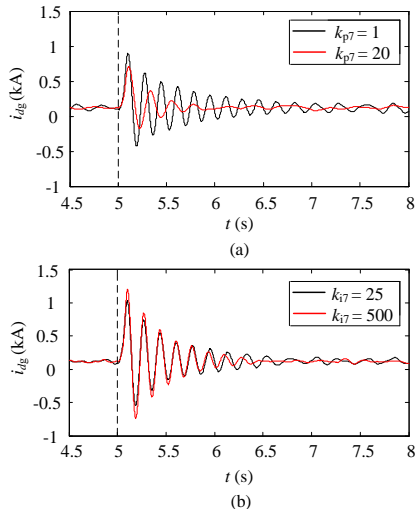

Fig. 18. Simulations results (i_{dg}) with the change of of k_{p7} and k_{i7} when a three-phase ground fault happens in the common bus at $t = 5$ s and it is cleared after 50 ms: (a) the impact of k_{p7} and (b) the impact of k_{i7}.

VI. CONCLUSION

In this paper, the SSO characteristics of direct-drive wind farms with VSC-HVDC systems are investigated based on the derived small-signal model. In addition, a new insight into the SSO mechanism is given by analyzing the interactions among the relevant state variables under the impact of controllers. The main conclusions are summarized as follows:

1) The X/R ratio of the collector cable impedance plays an important role in the SSO of the DDWFV. With the increase of the X/R ratio, the SSO is becoming severer.

2) To improve the SSO stability in the planning phase, the DC capacitance of the D-PMSG should be designed large, whereas the phase reactor of the VSC-HVDC should be small.

3) The impact of the VSC-HVDC connection on the system stability should consider both the control and AC-side characteristics. Different from the control characteristics, the AC-side characteristics provide negative damping.

4) A positive feedback system is formed under the impact of the DC voltage controller of the D-PMSG, which leads to instability. On the other hand, a negative feedback system is shaped under the impact of the DC voltage controller of the D-PMSG and the d-axis voltage controller of the VSC-HVDC, which mitigates the adverse effect of the positive feedback system. Thus, the SSO stability can be improved by increasing the gain of the negative feedback.

Moreover, it should be further noted that the SSO analysis in this paper assumes that the inverter of the VSC-HVDC is replaced with a DC voltage source. The SSO analysis considering the dynamic characteristics of the inverter will be the future work.

APPENDIX

The parameters of the DDWFV are shown in Tables A1 and A2.

TABLE A1
PARAMETERS OF EQUIVALENT D-PMSG POWER GENERATION SYSTEM

Modules	Parameters	Value
Wind turbine	Rated power (MW)	40×5
	Rated voltage (kV)	3
	Wind speed (m/s)	6
	Wind wheel radius (m)	58
	Air density (kg/m³)	1.225
	Rotor flux (Wb)	0.0417
	Number of pole pairs	49
	Stator resistance (Ω)	0.0950
	Stator inductance (H)	0.0121
	DC capacitor C (mF)	56
MSC	d-axis current reference i_{dsref} (kA)	0
	Speed reference ω_{sref} (rad/s)	37.699
	Unity power factor control coefficient (proportional k_{p1}, integral k_{i1})	1, 5
	Speed control outer loop coefficient (proportional k_{p2}, integral k_{i2})	0.4, 2.5
	Speed control inner loop coefficient (proportional k_{p3}, integral k_{i3})	1, 5
GSC	DC voltage reference u_{DCref} (kV)	5.0
	q-axis current reference i_{qgref} (kA)	0
	DC voltage control outer loop coefficient (proportional k_{p4}, integral k_{i4})	0.2, 285
	DC voltage control inner loop coefficient (proportional k_{p5}, integral k_{i5})	0.6, 2.5
	q-axis current control coefficient (proportional k_{p6}, integral k_{i6})	0.6, 2.5
PLL	Proportional k_{p_pll}, integral k_{i_pll}	5, 9
AC transmission lines	Filter inductor L_g (H)	0.002
	Resistance R_1 (Ω)	0.05
	Inductor L_1 (H)	0.001
	Capacitor C_1 (μF)	2
	Turns ratio 1: k (kV/kV)	3/35
	Turns ratio 1: k_2 (kV/kV)	35/110

TABLE A2
PARAMETERS OF VSC-HVDC

Modules	Parameters	Value
AC-side	Filter capacitor C_f (μF)	5
	Phase reactor L_{c1} (H)	0.015
REC	d-axis voltage reference u_{ds1ref} (kV)	89.815
	q-axis voltage reference u_{qs1ref} (kV)	0
	d-axis voltage control outer loop coefficient (proportional k_{p9})	0.0029
	q-axis voltage control outer loop coefficient (proportional k_{p10})	0.0029
	d-axis voltage control inner loop coefficient (proportional k_{p7}, integral k_{i7})	2.5, 10000
	q-axis voltage control inner loop coefficient (proportional k_{p8}, integral k_{i8})	2.5, 10000
DC-side	Resistance R_{dc} (Ω)	0.006
	Inductance L_{dc} (H)	0.0005
	Capacitor C_{dc} (μF)	150
	Equivalent DC voltage source u_{dc} (kV)	160

REFERENCES

[1] M. Dicorato, G. Forte, M. Trovato, E. M. Carlini, B. Aluisio, C. Gadaleta, and M. Migliori, "Transmission system and offshore wind farms: challenges and chances," in *Proc. EFEA*, 2018, pp. 1-6.

[2] A. B. Mogstad, M. Molinas, P. K. Olsen, and R. Nilsen, "A power

conversion system for offshore wind parks," in *Proc. IECON*, 2008, pp. 2106-2112.

[3] C. Li, P. Zhan, J. Wen, M. Yao, N. Li, and W. Lee, "Offshore wind farm integration and frequency support control utilizing hybrid multiterminal HVDC Transmission," *IEEE Trans. Ind. Appl.*, vol. 50, no. 4, pp. 2788-2797, Jul.-Aug. 2014.

[4] J. Yan, H. Lin, Y. Feng, X. Guo, Y. Huang, and Z. Q. Zhu, "Improved sliding mode model reference adaptive system speed observer for fuzzy control of direct-drive permanent magnet synchronous generator wind power generation system," *IET Renew. Power Gener.*, vol. 7, no. 1, pp. 28-35, Feb. 2013.

[5] C. Buchhagen, C. Rauscher, A. Menze, and J. Jung, "BorWin1 - First experiences with harmonic interactions in converter dominated grids," in *Proc. International ETG Congress 2015*, pp. 1-7.

[6] J. Lv, P. Dong, G. Shi, X. Cai, H. Rao, and J. Chen, "Subsynchronous oscillation of large DFIG-based wind farms integration through MMC-based HVDC," in *Proc. 2014 International Conference on Power System Technology*, 2014, pp. 2401-2408.

[7] C. Zou, H. Rao, S. Xu, Y. Li, W. Li, J. Chen, X. Zhao, Y. Yang, and B. Lei, "Analysis of resonance between a VSC-HVDC converter and the AC grid," *IEEE Trans. Power Electron.*, vol. 33, no. 12, pp. 10157-10168, Dec. 2018.

[8] Y. Xu, M. Zhang, L. Fan, and Z. Miao, "Small-signal stability analysis of type-4 wind in series-compensated networks," *IEEE Trans. Energy Convers.*, vol. 35, no. 1, pp. 529-538, Mar. 2018.

[9] S. Zhao, N. Wang, R. Li, B. Gao, B. Shao, and S. Song, "Sub-synchronous control interaction between direct-drive PMSG-based wind farms and compensated grids," *Int. J. Electr. Power Energy Syst.*, vol. 109, pp. 609-617, Jul. 2019.

[10] H. Liu, X. Xie, J. He, T. Xu, Z. Yu, C. Wang, and C. Zhang, "Subsynchronous interaction between direct-drive PMSG based wind farms and weak AC networks," *IEEE Trans. Power Syst.*, vol. 32, no. 6, pp. 4708-4720, Nov. 2017.

[11] Y. Li, L. Fan, and Z. Miao, "Wind in weak grids: low-frequency oscillations, subsynchronous oscillations, and torsional interactions," *IEEE Trans. Power Syst.*, vol. 35, no. 1, pp. 109-118, Jan. 2020.

[12] B. Huang, H. Sun, Y. Liu, L. Wang, and Y. Chen, "Study on subsynchronous oscillation in D-PMSG-based wind farm integrated to power system," *IET Renew. Power Gener.*, vol. 13, no. 1, pp. 16-26, Jan. 2019.

[13] M. Amin and M. Molinas, "Small-signal stability assessment of power electronics based power systems: a discussion of impedance- and eigenvalue-based methods," *IEEE Trans. Ind. Appl.*, vol. 53, no. 5, pp. 5014-5030, Sep.-Oct. 2017.

[14] K. Ji, G. Tang, J. Yang, Y. Li, and D. Liu, "Harmonic stability analysis of MMC-based DC system using DC impedance model," *IEEE J. Emerg. Sel. Top. Power Electron.*, vol. 8, no. 2, pp. 1152-1163, Jun. 2020.

[15] H. Zheng, L. Zhou, P. Sun, and W. Lu, "Large-signal stability analysis for VSC-HVDC systems based on mixed potential theory," *IEEE Tran. Power Deliv.*, vol. 35, no. 4, pp. 1939-1948, Aug. 2020.

[16] J. Z. Zhou, H. Ding, S. Fan, Y. Zhang, and A. M. Gole, "Impact of short-circuit ratio and phase-locked-loop parameters on the small-signal behavior of a VSC-HVDC converter," *IEEE Trans. Power Deliv.*, vol. 29, no. 5, pp. 2287-2296, Oct. 2014.

[17] L. P. Kunjumuhammed, B. C. Pal, C. Oates, and K. J. Dyke, "Electrical oscillations in wind farm systems: analysis and insight based on detailed modelling," *IEEE Trans. Sustain. Energy*, vol. 7, no. 1, pp. 51-62, 2014.

[18] K. Sun, W. Yao, J. Fang, X. Ai, J. Wen, and S. Cheng, "Impedance modeling and stability analysis of grid-connected DFIG-based wind farm with a VSC-HVDC," *IEEE J. Emerg. Sel. Top. Power Electron.*, vol. 8, no. 2, pp. 1375-1390, Jun. 2020.

[19] H. Zong, C. Zhang, J. Lyu, X. Cai, M. Molinas, and F. Rao, "Generalized MIMO sequence impedance modeling and stability analysis of MMC-HVDC with farm considering frequency coupling," *IEEE Access*, vol. 8, pp. 55602-55618, 2020.

[20] Y. Yu, X. Cheng, C. Zhang, and X. Ji, "Oscillation mechanism and mitigation of MMC-HVDC based on bifurcation theory for wind farm integration," *IEEE Access*, vol. 8, pp. 125121-125129, 2020.

[21] X. Wang and F. Blaabjerg, "Harmonic stability in power electronic-based power systems: concept, modeling, and analysis," *IEEE Trans. Smart Grid*, vol. 10, no. 3, pp. 2858-2870, May 2019.

[22] M. Cespedes and J. Sun, "Impedance modeling and analysis of grid-connected voltage-source converters," *IEEE Trans. Power Electron.*, vol. 29, no. 3, pp. 1254-1261, Mar. 2014.

[23] W. Du, B. Ren, H. Wang, and Y. Wang, "Comparison of methods to examine sub-synchronous oscillations caused by grid-connected wind turbine generators," *IEEE Trans. Power Syst.*, vol. 34, no. 6, pp. 4931-4943, Nov. 2019.

[24] Z. Yang, C. Mei, S. Cheng, and M. Zhan, "Comparison of impedance

model and amplitude-phase model for power-electronics-based power system," *IEEE J. Emerg. Sel. Top. Power Electron.*, vol. 8, no. 3, pp. 2546-2558, Sept. 2020.

[25] J. Lyu, X. Cai, and M. Molinas, "Frequency domain stability analysis of MMC-based HVdc for wind farm integration," *IEEE J. Emerg. Sel. Top. Power Electron.*, vol. 4, no. 1, pp. 141-151, Mar. 2016.

[26] J. Lyu and X. Cai, "Impact of controller parameters on stability of MMC-based HVDC systems for offshore wind farms," in *Proc. IET RPG 2015*, pp. 1-6.

[27] J. Lyu, X. Cai, and M. Molinas, "Optimal design of controller parameters for improving the stability of MMC-HVDC for wind farm integration," *IEEE J. Emerg. Sel. Top. Power Electron.*, vol. 6, no. 1, pp. 40-53, Mar. 2018.

[28] M. Amin, M. Molinas, and J. Lyu, "Oscillatory phenomena between wind farms and HVDC systems: The impact of control," in *Proc. COMPEL*, 2015, pp. 1-8.

[29] J. Lyu, M. Molinas, and X. Cai, "Stabilization control methods for enhancing the stability of wind farm integration via an MMC-based HVDC system," in *Proc. CPE-POWERENG*, 2017, pp. 324-329.

[30] M. Amin and M. Molinas, "Understanding the origin of oscillatory phenomena observed between wind farms and HVdc systems," *IEEE J. Emerg. Sel. Top. Power Electron.*, vol. 5, no. 1, pp. 378-392, Mar. 2017.

[31] H. Liu and J. Sun, "Voltage stability and control of offshore wind farms with AC collection and HVDC transmission," *IEEE J. Emerg. Sel. Top. Power Electron.*, vol. 2, no. 4, pp. 1181-1189, Dec. 2014.

[32] M. Amin and M. Molinas, "A gray-box method for stability and controller parameter estimation in HVDC-connected wind farms based on nonparametric impedance," *IEEE Trans. Ind. Electron.*, vol. 66, no. 3, pp. 1872-1882, Mar. 2019.

[33] M. Amin, A. Rygg, and M. Molinas, "Self-synchronization of wind farm in an MMC-based HVDC System: A stability investigation," *IEEE Trans. Energy Convers.*, vol. 32, no. 2, pp. 458-470, Jun. 2017.

[34] J. Lyu, X. Cai, M. Amin, and M. Molinas, "Sub-synchronous oscillation mechanism and its suppression in MMC-based HVDC connected wind farms," *IET Gener. Trans. Distr.*, vol. 32, no. 2, pp. 458-470, Feb. 2017.

[35] M. Cheah-Mane, L. Sainz, J. Liang, N. Jenkins, and C. E. Ugalde-Loo, "Criterion for the electrical resonance stability of offshore wind power plants connected through HVDC links," *IEEE Trans. Power Syst.*, vol. 32, no. 6, pp. 4579-4589, Nov. 2017.

[36] M. Cheah-Mane, J. Liang, N. Jenkins, and L. Sainz, "Electrical resonance instability study in HVDC-connected offshore wind power plants," in *Proc. IEEE PES General Meeting*, 2016, pp. 1–5.

[37] K. Ji, G. Tang, H. Pang, and J. Yang, "Impedance modeling and analysis of MMC-HVDC for offshore wind farm integration," *IEEE Trans. Power Deliv.*, vol. 35, no. 3, pp. 1488-1501, Jun. 2020.

[38] L. P. Kunjumuhammed, B. C. Pal, R. Gupta, and K. J. Dyke, "Stability analysis of a PMSG-based large offshore wind farm connected to a VSC-HVDC," *IEEE Trans. Energy Convers.*, vol. 32, no. 3, pp. 1166-1176, Sept. 2017.

[39] Y. Wang, C. Zhao, C. Guo, and A. U. Rehman, "Dynamics and small signal stability analysis of PMSG-based wind farm with an MMC-HVDC system," *CSEE J. Power Energy Syst.*, vol. 6, no. 1, pp. 226-235, Mar. 2020.

[40] W. Du, Q. Fu, and H. Wang, "Subsynchronous oscillations caused by open-loop modal coupling between VSC-based HVDC line and power system," *IEEE Trans. Power Syst.*, vol. 33, no. 4, pp. 3664-3677, Jul. 2018.

[41] K. Ji, H. Pang, J. Yang, and G. Tang, "DC side harmonic resonance analysis of MMC-HVDC considering wind farm integration," *IEEE Trans. Power Deliv.*, 2020. (Early access).

[42] L. Harnefors, M. Bongiorno, and S. Lundberg, "Input-admittance calculation and shaping for controlled voltage-source converters," *IEEE Trans. Ind. Electron.*, vol. 54, no. 6, pp. 3323-3334, Dec. 2007.

[43] S. Zhao and B. Shao, "An analytical method suitable for revealing the instability mechanism of power electronics dominated power systems," *Int. J. Electr. Power Energy Syst.*, vol. 109, pp. 269-282, Jul. 2019.

[44] J. Rocabert, A. Luna, F. Blaabjerg, and P. Rodriguez, "Control of power converters in AC microgrids," *IEEE Trans. Power Electron.*, vol. 27, no. 11, pp. 4734-4749, Nov. 2012.

[45] L.P. Kunjumuhammed, B.C. Pal, C. Oates, and K.J. Dyke, "The adequacy of the present practice in dynamic aggregated modeling of wind farm systems," *IEEE Trans. Sustain. Energy*, vol. 8, no. 1, pp. 23-32, Jan. 2017.

[46] K. Ogata, *Modern control engineering.* Upper Saddle River, NJ: Prentice hall, 2010, pp. 212.